

Lab on a Chip

Accepted Manuscript



This is an *Accepted Manuscript*, which has been through the Royal Society of Chemistry peer review process and has been accepted for publication.

Accepted Manuscripts are published online shortly after acceptance, before technical editing, formatting and proof reading. Using this free service, authors can make their results available to the community, in citable form, before we publish the edited article. We will replace this *Accepted Manuscript* with the edited and formatted *Advance Article* as soon as it is available.

You can find more information about *Accepted Manuscripts* in the [Information for Authors](#).

Please note that technical editing may introduce minor changes to the text and/or graphics, which may alter content. The journal's standard [Terms & Conditions](#) and the [Ethical guidelines](#) still apply. In no event shall the Royal Society of Chemistry be held responsible for any errors or omissions in this *Accepted Manuscript* or any consequences arising from the use of any information it contains.

Optofluidic Guiding, Valving, Switching and Mixing based on Plasmonic Heating in Random Gold Nanoisland Substrate†

Cite this: DOI: 10.1039/x0xx00000x

Received 00th January 2015,
Accepted 00th January 2015

DOI: 10.1039/x0xx00000x

www.rsc.org/

Jiajie Chen,^a Zhiwen Kang,^a Guanghui Wang,^{ab} Jacky Fong Chuen Loo,^c Siu Kai Kong,^c and Ho-Pui Ho^{*a}

We present a versatile optofluidic flow manipulation scheme based on plasmonic heating in random gold nanoisland substrate (Au-NIS). With its highly efficient conversion of optical power to hydrodynamic actuation, the reported substrate is used for laser-controlled optofluidics manipulation. It is the first time to realise microfluidic flow guiding, valving, and mixing within the same functional substrate. Plasmonic heating provides the power for guiding sample flow inside microfluidic channel at controlled speed and transportation of small particles or living cells are demonstrated. We have also made a laser-actuated microfluidic valve through controlling the surface wettability of the sample/Au-NIS interface. When the laser power density is sufficiently high to generate a bubble, localized convection around the bubble can lead to efficient sample mixing within a microfluidic chamber. The reported Au-NIS scheme practically offers a programmable functional surface on which users have the freedom to control the wetting characteristics with a focused laser beam. We have verified that this optofluidic approach induces insignificant degradation in cell viability. The reported scheme therefore offers a wide range of application possibilities in microfluidics and biomedical engineering, particularly those operating under a low Reynolds number.

Introduction

Localized surface plasmons (LSPs) are associated with the collective electron oscillations in metallic surfaces excited by incident light¹. LSPs have two distinctive features, i.e. efficient subwavelength confinement of optical energy down to nanometer scale and high sensitivity to the surrounding environment. These properties make LSPs a promising tool for nanoscale applications such as plasmonic trapping², surface enhanced Raman scattering³, biomedical sensing⁴, and optofluidics⁵. More recently, the plasmonic thermal effect has also been explored. The physical basis of this effect is easy to understand. When a metallic nanoparticle is excited at its resonant frequency, the electric current due to induced electron oscillations inside the metal particles are damped by lattice resistance, thus transferring the incident optical energy into thermal energy. The energy exchange process happens within nanoseconds after receiving the radiation, and the nanoparticle is heated up almost instantly⁶. For the case of heat transportation in surrounding the nanoparticles, the traditional Fourier heat conduction theory is no longer valid when the size of the nanoparticle is smaller than the mean free path of the heat carrier. This means that the temperature is higher inside the nanoparticle and heat carrier transport is nonlocal⁷. The plasmonic thermal effect has been used in several applications including heterogeneous catalysis⁸, particle trapping and manipulation⁹, localized heating in microfluidic chips¹⁰,

photothermal therapy¹¹. As the demand for miniaturization of biomedical testing devices has been increasing constantly over the years, a range of microfluidic sample manipulation techniques primarily based on complex electronic¹², ultrasonic¹³, or mechanical coupling schemes¹⁴ have been reported. Nanoscale heating facilitates the generation of abrupt temperature gradient which may lead to highly miniaturized hydrodynamic actuation in optofluidic systems. Common optofluidic systems tend to have low Reynolds number and microscale surface tension becomes the dominant force. Therefore, one have to deal with three major challenges: flow pumping, valving, and sample mixing. Extensive efforts have been made to resolve these issues, and schemes such as plasmon-assisted optofluidic pumping by adding gold nanoparticles into sample solution¹⁵, light controlled microfluidic valves via material phase switching^{16,17}, light-induced mixing in micro-channel^{18,19} have been studied. However, such techniques require either the addition of functionalizing gold nanoparticles to the sample which have to be removed by filtering before continuing with subsequent assay reactions, or restricted to specific locations where pre-fabricated structures are used for providing the solution mixing effect. Furthermore, as far as we know, we have yet to see any report on the use of a plasmonic substrate for addressing the aforementioned challenges within only one microfluidic system. In particular, the plasmon-assisted microfluidic valve demonstrated herein has never been studied before.

In this work, we show that plasmonic absorption in random distributed gold nanoisland substrates (Au-NIS) can be used efficiently as a microfluidic flow manipulation method for flow guiding, valving, switching and mixing. The random structures are prepared by a simple annealing process of a continuous gold film deposited on a glass substrate. The annealing step transforms the deposited gold coating into discrete gold nanoislands. The Au-NIS exhibits strong plasmonic resonance characteristics with the absorption peak readily tunable by adjusting the annealing temperature. In fact, the morphology and plasmonic properties of Au-NIS have been studied comprehensively elsewhere²⁰⁻²². However, the wettability of water on Au-NIS has rarely been explored. In this paper, we characterized the surface wettability of the Au-NIS by measuring the contact angles in samples prepared under different annealing conditions. The results have strong correlation with the speed of the guided flow in our optofluidic experiments. The guided flow action is achieved by focusing a laser beam through the backside of the Au-NIS. Plasmonic localized heating perturbs the wettability of the Au-NIS surface, which results in guiding an aqueous sample to move along a micro-channel, and the channel is formed by bonding a moulded PDMS block²³ to the Au-NIS surface. The direction and speed of the guided flow are fully controlled by the movement and power of the focused laser beam. Typically only several milliwatts of laser power is required for a 20 μm diameter spot size. This same plasmonic heating strategy is also used for laser-controlled optofluidic valving and switching. In addition, because of the strong optothermal response from the Au-NIS, higher laser power results in the formation of an air bubble on the Au-NIS. Most importantly, the bubble-Au-NIS interface can act as a mixing pump in small dimensions at any locations of interest.

This miniaturized optofluidic system is much smaller than the common lab on a disk (LOAD) platform, not only can it be integrated with LOAD platform to improve its performance, but also can be fabricated on a coin size chip to independently conducting ordinary biomedical analysis or cellular manipulation. Besides, this platform is all embedded on a microscope (Eclipse TE2000-U), thus, facilitates the observation of specific biochemical reaction and also make it easy for other detection system to connect with, such as Raman spectrometer or fluorescence microscopy, hence, it is very promising to be used for in-situ detection of solution based reactions.

Materials and methods

1. Substrates preparation

In the experiment, five identical cover glasses (Prod No. 260140, 22×22 mm² × 0.13~0.16 mm thick; Ted Pella Inc.) were coated with 5 nm gold film using thermal evaporation deposition system (Edwards, UK). The base pressure was 10⁻⁶ Torr and the deposition rate is 0.1 Å/s, and monitored by a quartz crystal microbalance (Maxtek Inc.). After the deposition of the gold film, four of them were annealed for 12 minutes at the temperatures of 100 °C, 200 °C, 300 °C, and 600 °C respectively. All samples were stored in an electronic drying cabinet (WEIFO Inc.). SEM images confirmed that the thermal annealing process transformed the gold film from a percolated morphology to two-dimensional discontinuous faceted nanoislands (Fig.1). Depending on the annealing temperature, the nanoislands had sizes ranging from 20 nm to 100 nm. Consequently, we were able to tune the location of the

absorption peak between 536 nm and 753 nm within the extinction spectrum as shown in Fig. 1(f).

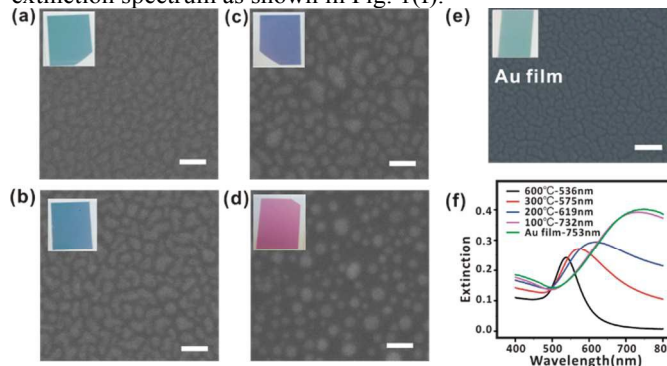


Fig.1 SEM images of four Au-NIS samples produced with different thermal annealing temperatures: (a) S1: 100°C; (b) S2: 200°C; (c) S3: 300°C; (d) S4: 600°C. (e) S0: As-deposited gold film with no annealing treatment. (f) Extinction peaks of the five samples. The scale bar is 100 nm.

2. Fabrication of polydimethylsiloxane (PDMS) micro-channel samples

Master fabrication. In order to investigate the optofluidic control characteristics of plasmonic absorption, we monitored the guided flow properties as we varied the spot size of the focused laser beam and the width of the microfluidic channel. In all cases, the laser spot size, which was between 20 and 35 μm , was chosen to be comparable with the channel width. Furthermore, shallow channels were used in order to suppress convective flow⁵. Shallow channels also favor the use of photolithography for the fabrication of our devices. The microfluidic channels width is in the range between 30 and 80 μm . The design was first printed on high-resolution plastic film, which served as the photolithographic mask. A positive photoresist (AZ4620, AZ Electronic Materials, HK) was patterned on a silicon wafer to create the master. After priming the wafer with bis(trimethylsilyl)amine (HMDS), a layer of spin-coated positive photoresist was applied to the wafer surface by first spinning at 500 rpm for 5 s, followed by 2000 rpm for 30s, and finally 3000 rpm for 4s. The resist-coated wafer was baked at 90 °C in an oven for 1 minute. After cooling the wafer to room temperature, UV contact printing was conducted with an exposure time of 20 s. Finally, the photoresist was developed in a solution (AZ400K: DI water= 1: 4 by volume) for 3 minutes. After rinsing in DI water and blow dry, the final thickness of the master was 10 μm . For the study of valving and mixing, deeper channels are more suitable to facilitate liquid flow and the formation of bubbles. It was not necessary to use high-resolution photolithography, and we fabricated the master on a PMMA substrate with micro engraving (Kingcut, Creation Technology, HK).

Molding. We first mixed PDMS pre-polymer with a curing agent (15: 1 by volume, Sylgard 184, Dow Corning, Midland, MI). After degassing under vacuum, the mixture was poured onto the master and cured at 70°C for 3h. The cured PDMS replica was peeled from the master. Immediately after that, the replica was attached to the as-prepared Au-NIS. Van de Waal adhesion between PDMS and the Au-NIS surface was sufficient to prevent any leakage from the micro-channels.

3. Surface wettability measurement

Fig. 2 shows that as we increased the annealing temperature, the contact angle of the Au-NIS became smaller, which means a better surface wettability. This trend can be explained by the fact that higher annealing temperature resulted in lower density of gold nanoislands on the glass surface, enlarging the portion of exposed glass area which is hydrophilic, as shown in Fig. 2 (e) and (f), thus making the sample better surface wettability. Moreover, Fig. 2 (g) also confirms that the contact angle of unmodified PDMS surface is hydrophobic.

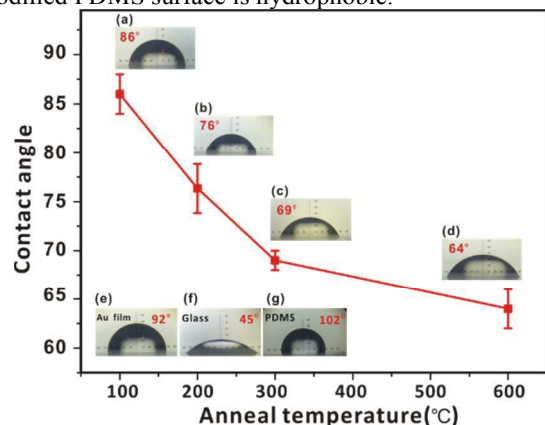


Fig. 2 Contact angles of four Au-NIS samples produced with different thermal annealing temperatures. (a) S1: 100°C; (b) S2: 200°C; (c) S3: 300°C; (d) S4: 600°C. Contact angles of other relevant materials. (e) S0 : As-deposited gold film with no annealing treatment. (f) Glass substrate. (g) PDMS. Error bars are standard deviations of three measurements for each data points.

4. Measurement of absorption induced temperature changes

To ensure that we had an accurate picture of the microscopic temperature distribution around the laser illuminated spot where plasmonic absorption takes place, we made use of the fluorescent-temperature relationship of Rhodamine B (0.1 mM) to measure the temperature¹⁰. This method also provided information on the average temperature of the entire illuminated region (laser spot diameter is 20 μm). In the experiment, the room temperature was 21 $^{\circ}\text{C}$, and after the pre-calibration and data fitting, we obtained the final temperature measurement of the hot-zone in the laser-illuminated spot.

Temperature ($^{\circ}\text{C}$) \ \ power (mW)	P1 (1.5m W)	P2 (5.0m W)	P3 (12.0m W)	P4 (20.0m W)	P5 (52.0m W)
S0 (No annealing)	21.7 \pm 0.2	23.3 \pm 0.3	25.6 \pm 0.3	bubble	bubble
S1 (100 $^{\circ}\text{C}$ annealing)	21.6 \pm 0.3	22.9 \pm 0.4	25.3 \pm 0.5	bubble	bubble
S2 (200 $^{\circ}\text{C}$ annealing)	21.3 \pm 0.2	22.4 \pm 0.3	24.3 \pm 0.4	bubble	bubble
S3 (300 $^{\circ}\text{C}$ annealing)	20.9 \pm 0.1	21.7 \pm 0.3	23.1 \pm 0.3	24.5 \pm 0.6	bubble
S4 (600 $^{\circ}\text{C}$ annealing)	20.8 \pm 0.2	21.0 \pm 0.2	21.2 \pm 0.2	21.4 \pm 0.2	22.0 \pm 0.3

Table 1. Temperature measurement of S0-S4 in different laser powers. The data with their standard deviations are the average temperatures

measured around the laser illuminated region. And “bubble” means the generation of air bubble.

As shown in Table 1, a higher temperature was observed from the substrate whose absorption peak was close to the laser line (785nm) because of more efficient optical absorption via the non-radiative damping of LSP in the gold nanoparticles. The temperature data shown in this table are the average values over a detection area of 220 μm \times 165 μm . In addition, the temperature profile of this region, as shown in Fig. 3, carries the same Gaussian distribution as the laser beam. Since the aqueous sample was in direct contact with the Au-NIS surface, its temperature increased immediately after receiving optical energy from the laser. If the power level was sufficiently high, the system was able to reach steady-state temperature within 250 ms, which is comparable to microfluidic heating devices previously reported¹⁰. For a laser power of 12 mW, the highest temperature within the laser-illuminated region was 64 $^{\circ}\text{C}$. As we further increased the laser power (e.g. 20 mW for S1, 52 mW for S3), absorption in the Au-NIS was able to induce boiling of water that finally led to the generation of an air bubble above the surface. Our data agreed with those reported in Ref. 24 and Ref. 6, which revealed that the high temperature region was only within the 100 nanometers from the substrate surface, while the overall average temperature change was only around 10 $^{\circ}\text{C}$ which was not significant. Therefore it has little influence to the particles and cells in the bulk solution.

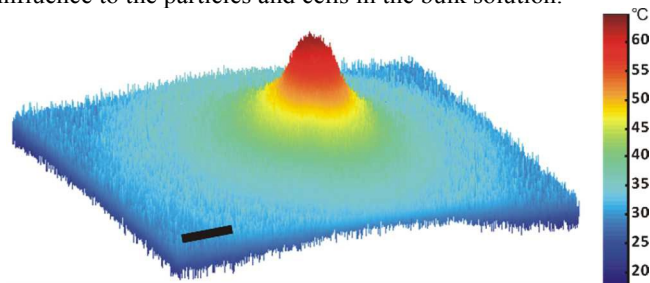


Fig. 3 Temperature distribution around the laser illuminated region within an area of 220 μm \times 165 μm . Substrate: S1; 785 nm laser power: 12 mW; scale bar: 35 μm .

Results and discussion

1. Au-NIS based optofluidic control

We systematically studied the performance of the substrates for optofluidic control. Fig. 4 shows the experimental setup. The PDMS channel was attached to the surface of the Au-NIS naturally under Van de Waal force. The height of the channel was 10 μm , with widths ranging from 30 to 80 μm . A 785nm diode laser was focused at leading edge of meniscus as we half-filled the microchannel with water. Heat generated at the Au-NIS-water interface consequently guided the flow as we moved the laser spot along the channel.

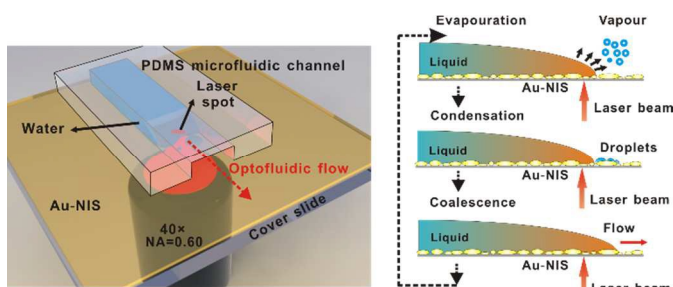


Fig. 4 Optical setup and operation principle of flow guiding assisted by plasmonic absorption.

The physics of various liquid advancing process has been widely studied by experiment¹⁵ as well as simulation²⁵, thus providing us a comprehensive understanding on the flow mechanism. In the present case, as shown in Fig. 4, when the laser spot is directed focus at the meniscus region, a small amount of water is evaporated due to plasmonic absorption in Au-NIS. The vapor then condenses into droplets immediately in front of the meniscus. Shortly afterwards, more water is vaporized, and the droplets grow larger. When they have reached a sufficiently large size, they coalesce to form a continuous water column, thereby advancing the water boundary to a new location. This sequence of steps continuous as one moves the laser spot along the channel, as long as there is sufficient time for the droplets to grow and coalesce. Fig. 5 shows the operations of water being accurately guided by the 785nm laser spot into selected microchannels with different widths. And the video of the flow guiding is shown in Supplementary Information Movie S1.

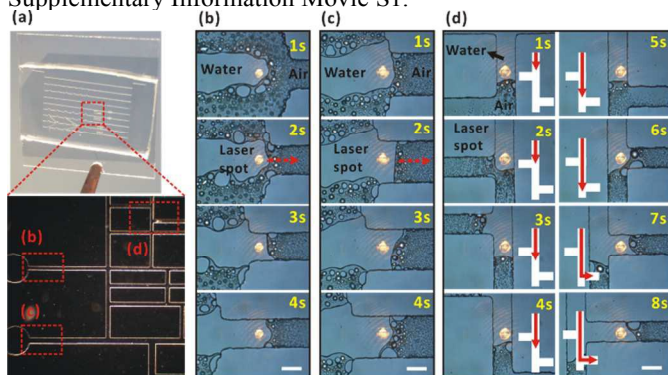


Fig. 5 (a) Microchannel sample and temporal sequences on sample S2 with 5 mW 785nm laser. (b) 60 μm wide channel with guided flow rate 40 $\mu\text{m}/\text{s}$. (c) 80 μm wide channel with guided flow rate 20 $\mu\text{m}/\text{s}$. (d) Selected flow into a specific exit channel after a sharp turn. Channel width: 40 μm . All scale bars are 40 μm .

In this guided flow process, since the evaporation rate is proportional to the incident laser power, one can readily see that for a given laser power there exists a maximum continuous flow guiding speed. On the other hand, factors including surface wettability, channel width, and Au-NIS extinction peak will also influence the operation. We conducted a correlation investigation on the guided flow maximum speed in relation to other parameters. The laser power we used was ranged from 1.5 to 52 mW, the corresponding power density was from 4.8 to 165.6 $\mu\text{W}/\mu\text{m}^2$. Fig. 6 shows the maximum speed of the guided optofluidic flow in relation to various operational and design

parameters. Fig. 6 (a) indicates that thinner channel width leads to higher maximum speed. This is attributed to faster heating rate caused by a reduction in the fluid volume interacting with the laser spot. Fig. 6 (b) shows the comparison of maximum speed between different substrates with the same channel width, while Fig. 6 (c) shows the difference between 532nm and 785nm laser lines in the Au-NIS sample annealed at 600 $^{\circ}\text{C}$, which has an extinction peak closer to the 532 nm laser. The result confirms that for samples having an extinction peak closer to the laser line, the maximum flow speed becomes higher due to increased opto-to-thermal power conversion efficiency. We also conducted a control experiment on a bare glass substrate without Au coating, and no laser flow guiding was observed.

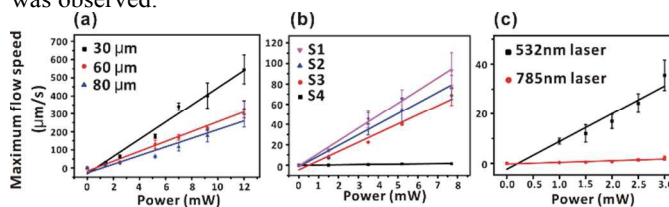


Fig. 6 (a) Maximum fluid flow speed versus illumination power from 785nm laser in sample S1. (b) Maximum flow speed in 80 μm wide channel versus 785nm laser power for the four samples that underwent different annealing temperatures. (c) Maximum flow speed in 80 μm wide channel versus illumination power from two lasers (532 nm & 785 nm) in sample S4. The solid lines represent a linear fit of the data. Error bars are standard deviations of three measurements for each data points.

Our experiment also revealed that when the laser power was under 12 mW, the maximum flow speed had linear relationship with the incident optical power. With higher laser power levels, it was possible to induce the formation of a gas bubble on the substrate, which then resulted in a blockage of the flow. Nonetheless, the maximum guided flow speed in a 30 μm wide channel can be as high as 1600 $\mu\text{m}/\text{s}$ from an Au-NIS sample annealed at 300 $^{\circ}\text{C}$ upon receiving 20 mW of 785nm laser power. Indeed this flow speed was much higher than those obtained from other substrates. Our study also reveals that the level of maximum flow speed is related to two effects: (i) opto-to-thermal conversion efficiency and (ii) wettability of the surface. For the aforementioned case, the opto-to-thermal conversion factor played a more significant role. The sample that underwent 300 $^{\circ}\text{C}$ annealing was the second most hydrophilic sample as compared to the one annealed at 600 $^{\circ}\text{C}$, while its extinction peak was closer to the 785nm laser line. On the other hand, as seen from Table 1, although the laser induced temperature changes were almost the same for the cases of 20 mW on the sample annealed at 300 $^{\circ}\text{C}$ and 12 mW on the sample anneal at 200 $^{\circ}\text{C}$ (highlighted in boldface), a higher maximum flow speed was achieved in the former on due to its relatively higher degree of wettability.

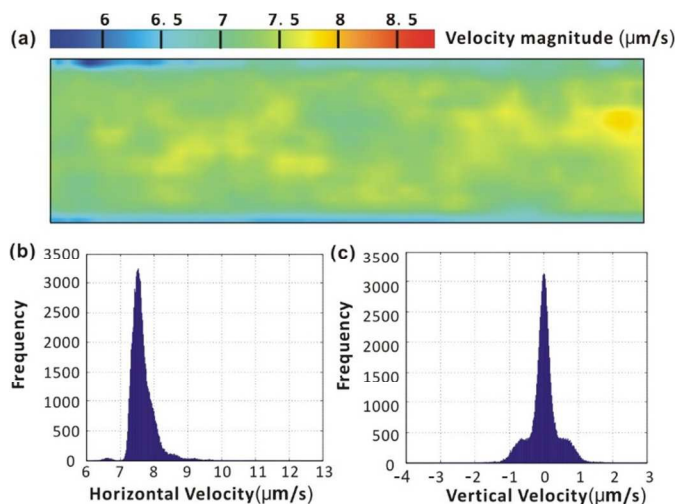


Fig. 7 Particle image velocimetry analysis from 235 successive image frames. (a) Velocity magnitude distribution in the 80 μm channel. The velocity of the guiding laser spot is 7.5 $\mu\text{m/s}$. (b) Statistic of particles horizontal velocity in the channel. (c) Statistic of particles vertical velocity in the channel.

In addition, we successfully demonstrated guided flow of suspensions containing 1 μm polystyrene beads or *E. coli* cells in the micro-channel on S0 substrate, and the results are shown in Supplementary Information Movie S2. The suspended contents (particles or cells) can be transported with a laser beam inside the channel smoothly without any observable changes to their physical characteristics. To quantify this, we use a particle tracking program based on cross-correlation and relaxation algorithms to study the velocity distribution in the channel²⁶. As shown in Fig. 7, the average horizontal speed of the particles in the medium is almost identical to the laser speed and the situation remains the same with other laser speed. The vertical (i.e. perpendicular to the flow direction) velocity distribution is axisymmetric, thus indicating that Brownian motion induces the same degree of turbulence on particle motions. Moreover, we monitor the particle density distribution as the sample having undergone laser guided flow over a long distance. The results are shown in Fig. 8. As a control experiment, the variation of particle density associated with pressure-actuated flow is recorded. Polynomial fit of the two sets of experimental results indicates that both laser guided and pressure actuated cases follow the same trend, i.e. particle density decreases with distance of travel. We attribute this to the fact that some of the particles near the channel wall become stationary or immobilized because of reduced particle speed as they are near or inside the stagnant boundary layer. In both cases, laser guided and pressure actuated flow, the density gradient along the length of the channel will drive the particle toward a homogeneous state within about 15 minutes.

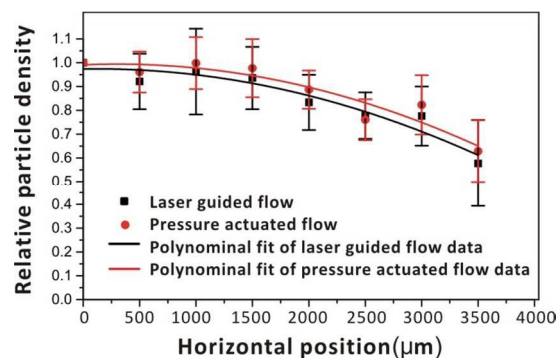


Fig. 8 Particle density monitoring plots after the particles have travelled for a distance of 3500 μm . The relative particle density is the ratio of the current density to the density at starting position. Each curve point is the average of 8 measurements from a flow speed from 7 $\mu\text{m/s}$ to 200 $\mu\text{m/s}$ with different channel widths, and the error bar indicates the standard deviation. Polynomial fit of these data points help us to see the trend.

In summary, we have demonstrated that one can readily customize the characteristics of the guided flow device by adjusting the sample treatment conditions, microchannel width, laser line, and laser power. The experimental maximum flow speed can be anywhere between 0 and 1600 $\mu\text{m/s}$. This range is much wider than that obtained by dispersing suspended metal nanoparticles in the sample solution¹⁵ while with less optical power consumption.

2. Au-NIS based optofluidic valving and switching

Because of the reported possibility to perturb surface wettability in Au-NIS by a laser beam, we have further adapted the plasmonic absorption effect for optofluidic valving and switching applications. Until now, such optofluidic operations are based on light-induced melting of paraffin wax^{16, 27} or hydrogel²⁸, or shape changes of polymer foil¹⁷. These approaches have the drawbacks of single use and chemical resistance of the valving material. Moreover, recently an optofluidic valve based on plasmonic heating has been reported²⁹. Although the plasmon-enabled photothermal conversion is highly efficient, this kind of valve is only active with a thermo rheological fluid, which poses severe limitation on its use for water-based biochemical reactions. Here, the reported approach is purely a physical effect associated with a chemically resistant refractory metal that have been deposited at selected locations on the microfluidic device platform. The scheme can be used for capillary burst valves, flow direction switch and pressure regulators, with reasonability reproducible burst conditions³⁰. And it is most suitable for integration with a device to support water-based biochemical applications. Since the as-deposited Au-NIS surface (without thermal anneal) is hydrophobic, while the bare glass surface is hydrophilic, we can easily form a gate valve by depositing a narrow strip of Au nanoislands across a microchannel as shown in Fig. 9. The gate valve will be released by directing a focused laser beam at the strip. A simple analysis on the operation of this gate valve, as shown in Fig. 9 (a), is presented below.

For a water-filled microchannel with the flow stopped at the abrupt expanding region, the system satisfies the following conditions³⁰:

$$P_w \leq P_c = 4\gamma_{al} \sin \theta_c / D_h \quad (1)$$

Where P_w is water pressure, P_c is critical burst pressure, γ_{al} is surface energy per unit area of the liquid–air interface, θ_c is equilibrium contact angle, and D_h is hydraulic diameter. The hydraulic diameter of a rectangular channel is:

$$D_h = \frac{2wh}{w+h} \quad (2)$$

Where w and h are the width and height of the channel. When the focused laser beam illuminates the water meniscus, the water boundary will advance a small distance and fill the abruptly expanded channel. Consequently the hydraulic diameter D_h is larger now because of the increase of channel width w , thus leading to a drop of the critical burst pressure P_c , as indicated in equation (1). While the water pressure P_w remains constant, a break in pressure balance occurs, finally water will burst into the exit flow channel. In our experiment, the critical burst pressure was slightly higher than the theoretical value. We attribute this to the fact that the Au-NIS region is hydrophobic, which has added an extra component, i.e. surface tension, to the overall burst pressure requirement³¹.

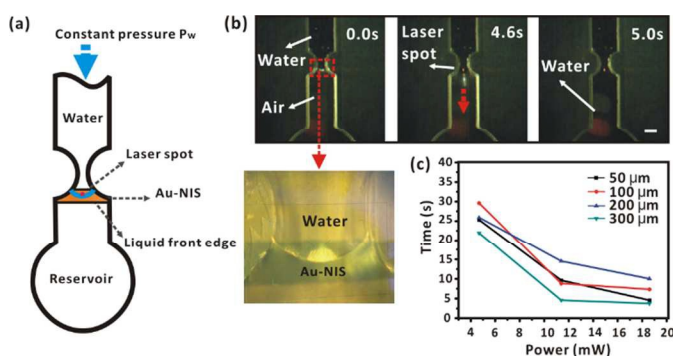


Fig. 9 (a) Schematic of valving operation driven by 785nm laser. Constant pressure is supplied from a raised container filled with water. (b) Temporal sequence of a 300 μm wide microfluidic valve controlled by 12 mW 785 nm laser. The beam is focused by an objective (20 \times , 0.45 NA, Olympus) to a diameter of 35 μm . The Au-NIS strip has a width of 150 μm . (c) Valve opening time versus laser power for different valve widths ranging from 50 to 300 μm . The height of all channels is 500 μm . The scale bar is 500 μm .

Fig. 9 (b) shows the temporal sequence of this operation. Moreover, as highlighted by Fig. 9(c), we also studied the valve actuation time, i.e. time delay between the laser power on and the moment when water start to flow through the valve, versus laser power for different widths of the Au-NIS region (see Supplementary Information, Movie S3, S4). A higher laser power can speed up the vaporizing process, thus leading to shorter actuation time. In another experiment, we combined two such valves together to form a “Y” junction in order to achieve the function of optofluidic switching. As illustrated by Fig. 10, the laser beam can be used to selectively open a specific channel to enable passage of liquid contents in to the Y-junction (see Supplementary Information, Movie S5).

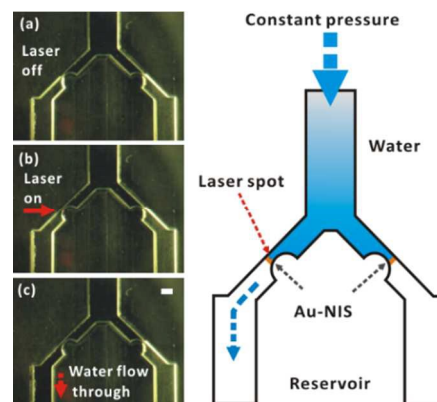


Fig.10 Temporal sequence of optofluidic switching. (a) The fluidic channel is blocked by two valves along the “Y” junction. (b) The 20 mW 785nm laser beam is focused directed at the valve on the left hand side by a $\times 40$ objective. The minimum channel width is 50 μm . (c) After opening the valve by an incident laser, water flows through. The scale bar is 500 μm .

In terms of power density requirement, the minimum level to actuate our valve was 1.04 $\mu\text{W}/\mu\text{m}^2$ with total incident laser power of 4.7 mW. When the incident power was increased to a maximum of 52 mW, with a 300 μm channel width, an actuation time as short as 2.4 seconds was achieved. Typically, the power of 10 to 20 mW was sufficient, which resulted in an actuation time between 3.8 and 10.1 seconds. The power density requirement compares very favorably with optofluidic valving devices previously reported^{17, 32} while response time has not been compromised. In addition, the actuation of this Au-NIS based valve does not require any chemical material to undergo phase change.

3. Au-NIS based optofluidic mixing/stirring

With sufficiently high incident laser power, plasmonic absorption in the Au nanoislands may lead to ideal nano heaters. When the water around the gold nanoparticles becomes overheated, the dissolved air will be release to form an air bubble directly above the hot zone³³. Soon after switching off the laser bubble will diminish and finally disappear within a few minutes. After the air bubble has reached its equilibrium size, strong convective flow of water takes place around the interface region between the bubble and the Au-NIS. Indeed such a strong convective flow can be used for the manipulation of particles in the water medium⁹. It is well-known that solution mixing is relatively difficult in the micro scale because of the low Reynolds number involved. Recently, bubbles have also been utilized to assist microfluidic mixing. Pneumatically generated bubbles³⁴, acoustically induced bubbles³⁵ and high power laser induced bubbles³⁶ for microfluidic mixer have been reported. However, long mixing channels, complex channel designs or high laser power levels are required. Here, we demonstrate the use of convective flow induced by the air bubble for free-range micro scale stirring.

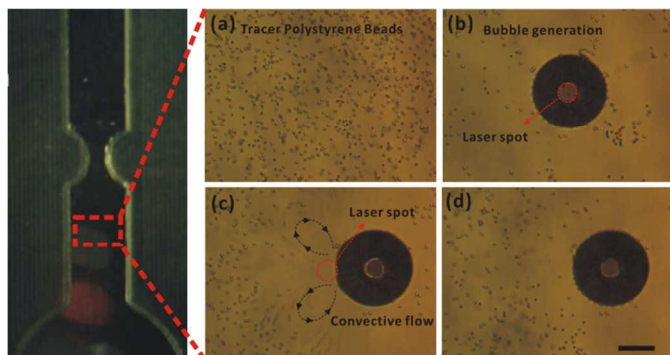


Fig.11 Experimental details of optofluidic stirring. (a) Tracer polystyrene beads are suspended in the PDMS chamber with a height of 500 μm . (b) A bubble is generated within 0.5 s by focusing a 52 mW 785nm laser at the Au-NIS. (c) To sustain a stable convective flow, lower power level (12 mW) from the 785nm laser was used. The bubble diameter is $\sim 80 \mu\text{m}$ and laser spot diameter is $\sim 20 \mu\text{m}$. (d) No convective flow after switching off the laser. The scale bar is 40 μm .

In the experiment, the height of PDMS chamber was 500 μm , a 5 nm Au-NIS without thermal annealing was used as the substrate (extinction peak at 752 nm). We added polystyrene beads (diameter 1.5 μm) into the water to act as tracers of the convective flow. As shown in Fig. 11, once the 52 mW 785nm laser was focused at the Au-NIS and water interface, due to strong plasmonic absorption, the water immediately heated at the laser-illuminated region and finally an air bubble was formed. Continuous laser illumination at this power level could increase the size of the bubble and the temperature around the hot zone become very high³², which may lead to some side effect to the substrate as well as the suspended particles. Typically we reduced the power level from 52 mW to around 12 mW as soon as the formation of an air bubble was achieved. The laser spot was moved within a short distance to the interface zone between the air bubble and the water in order to generate the required convective flow, as shown in Fig. 12 (c). This procedure was highly reproducible. Our result agrees well with those report from previous work in which a spot heater located around a water-air interface will generate convective flow for optofluidic mixing¹⁹. As soon as we switch off the laser, the convective flow stopped and the bubble disappeared within 5 minutes. Details of our procedures are shown in Supplementary Information Movie S6. With this Au-NIS approach, one can easily generate bubbles as well as optofluidic mixing on the sample surface at any location as desired. Localized fluidic mixing enabled by this technique will be very suitable for high-density lab-on-a-chip systems.

4. Verification of cell viability after the experiment

To evaluate whether cells manipulated by this plasmonic optofluidic technique may suffer possible degradation in viability or proliferation, we conducted a series of flow guiding and mixing experiments on 20 μl of Bacteria *E. coli* solution (OD 600 =1) with a 785 nm laser at different power levels for 10 minutes. Two follow-up assays were performed to evaluate the cell viability in terms of growth rate and membrane integrity.

For growth rate, the bacteria used in the optofluidic experiments with and without laser guided flow were incubated

in fresh LB medium at 37°C at 150 rpm for various time intervals and absorbance for cell density in medium was measured at 600 nm (OD 600). From the results shown in Fig. 10 (a), the bacteria growth rates for the different power levels overlap with each other, thus implying that there is no observable change of growth property or number of initial alive cells in all cases. Also, the bacteria average doubling times for no laser treatment, low laser power, medium laser and high laser groups are respectively $1.20 \pm 0.32 \text{ h}$, $1.10 \pm 0.35 \text{ h}$, $1.61 \pm 0.75 \text{ h}$ and $1.09 \pm 0.34 \text{ h}$. Indeed, there is no significant difference in growth rate between these groups.

To measure membrane integrity, the bacteria after having gone through laser guided flow were stained with both green fluorescent dye (SYTO-9, 5 μM) and red fluorescent dye (Propidium iodide (PI), 30 μM), based on the fact that PI can pass through a leaky membrane and only dead cells can be stained, with a higher affinity, PI competes for the nucleic acid binding sites with SYTO-9 thereby giving a lower green fluorescence signal in dead cells³⁷. Fig. 10 (b) shows the fluorescence emission detected by Tecan Safire Fluorescence Scanner from 510 to 655 nm with an excitation at 470 nm after labeling. Green/Red ratio was then calculated using the fluorescence value at 530 nm/635 nm to show the relative viability, a low ratio indicates a low viability. As shown in Fig. 10 (c), The results for different laser power levels exhibit no significant difference as compared to that of the no laser control group, while heat-killed bacteria positive control (10 minutes boiling of bacteria) show significant difference with $p < 0.001$ in statistical student t-test. The results indicated that the bacteria did not suffer any observable damage. Hence, by combining this result with the fact there is no significant difference in growth rate we can conclude that the bacterial intracellular replication mechanism was not disrupted in this optofluidic manipulation process.

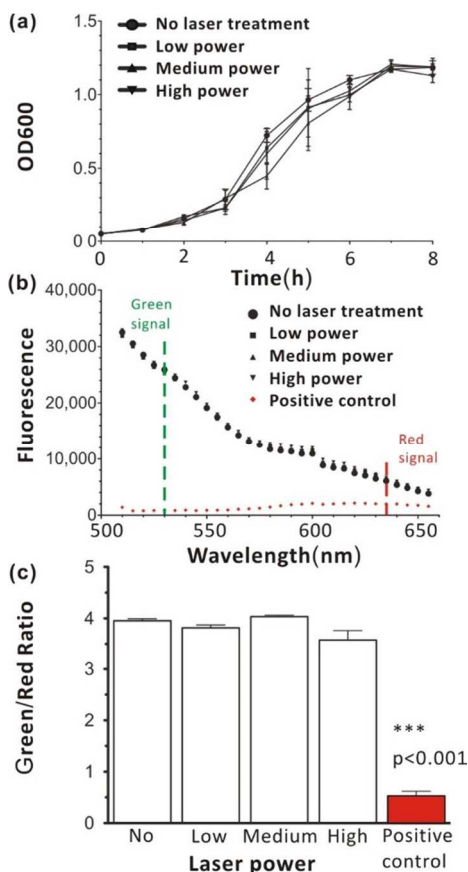


Fig.12 Effect of laser guided flow on bacterial viability. The corresponding laser powers used here are low power =5 mW, medium power =12 mW, and high power =52 mW (a) Bacteria growth plots for different power levels. (b) Fluorescence emission spectrum of the stained *E. coli* under different treatments. (c) Green/Red fluorescence ratio (530 nm/635 nm) of the five groups. Results are mean \pm SEM ($n=3$ independent experiments), student t-test was performed, *** $p < 0.001$.

Conclusion

In this paper, for the first time we demonstrate optofluidic applications based on the use of plasmonic absorption in random distributed Au nanoislands. Also for the first time the surface wettability of the Au-NIS has been studied. Based on the surface wettability change induced by plasmonic heating, we have achieved optofluidic flow guiding with living cells transportation and a laser-controlled valving scheme. We have also demonstrated a localized optofluidic mixing strategy at any location of interest. The reported plasmonic optofluidic approach offers a higher degree of versatility than the techniques previously reported, and the preparation of Au-NIS only requires simple thermal annealing steps. This Au-NIS based optofluidic scheme offers a general strategy for various functional microfluidic operations including pumping, valving, switching, mixing, and other fluidic sample manipulation devices. It is inherently compatible with other optical detection or spectroscopy techniques, thus leading to further application opportunities in high-density lab-on-a-chip and all optical biomedical optofluidic detection and sensing devices, which are yet to be fully explored.

Acknowledgements

The authors acknowledge the financial support from the CRF scheme (CUHK1/CRF/12G), the AoE scheme (AoE/P-02/12) and a GRF project (412613) from the Research Grants Council (RGC) of Hong Kong Special Administrative Region, China. And also acknowledge the help from Jingjing Liu, Lijia Zou, Shu-Yuen Wu in Solid State Lab of The Chinese university of Hong Kong.

Notes and references

^a Department of Electronic Engineering, The Chinese University of Hong Kong, Shatin, Hong Kong, P. R. China.

^b Institute of Optical Communication Engineering, Nanjing University, Nanjing, 210093, P. R. China.

^c Department of Biochemistry, The Chinese University of Hong Kong, Hong Kong SAR, PR China.

† Electronic Supplementary Information (ESI) available. See DOI: 10.1039/b000000x/

- 1 E. Hutter and J. Fendler, *Advanced Materials*, 2004, **16**, 1685-1706.
- 2 B. J. Roxworthy, K. D. Ko, A. Kumar, K. H. Fung, E. K. Chow, G. L. Liu, N. X. Fang, and K. C. Toussaint, *Nano letters*, 2012, **12**, 796-801.
- 3 A. M. Michaels, M. Nirmal, L. E. Brus, *Journal of the American Chemical Society*, 1999, **121**, 9932-9939.
- 4 J. R. Guerreiro, M. Frederiksen, V. E. Bochenkov, V. De Freitas, M. G. Ferreira Sales, and D. S. Sutherland, *ACS nano*, 2014, **8**, 7958-7967.
- 5 J. Donner, G. Baffou, D. McCloskey, and R. Quidant, *ACS nano*, 2011, **5**, 5457-5462.
- 6 X. Chen, Y. Chen, M. Yan, and M. Qiu, *ACS nano*, 2012, **6**, 2550-2557.
- 7 G. Chen, *Journal of Heat Transfer*, 1996, **118**, 539-545.
- 8 J. Adleman, D. Boyd, D. Goodwin, and D. Psaltis, *Nano letters*, 2009, **9**, 4417-4423.
- 9 C. Zhao, Y. Xie, Z. Mao, Y. Zhao, J. Rufo, S. Yang, F. Guo, J. Mai, and T. Huang, *Lab on a Chip*, 2014, **14**, 384-391.
- 10 Z. Li, P. Wang, L. Tong, and L. Zhang, *Optics express*, 2013, **21**, 1281-1286.
- 11 X. Huang, P. Jain, I. El-Sayed, and M. El-Sayed, *Lasers in Medical Science*, 2007, **23**, 217-228.
- 12 A. Wu, L. Wang, E. Jensen, R. Mathies, and B. Boser, *Lab on a chip*, 2010, **10**, 519-521.
- 13 P. Rogers, I. Gralinski, C. Galtry, and A. Neild, *Microfluidics and Nanofluidics*, 2012, **14**, 469-477.
- 14 J. Wang, M. J. Stine, and C. Lu, *Analytical chemistry*, 2007, **79**, 9584-9587.
- 15 G. Liu, J. Kim, Y. Lu, and L. Lee, *Nature Materials*, 2005, **5**, 27-32.
- 16 K. Abi-Samra, R. Hanson, M. Madou, and R. Gorkin, *Lab on a chip*, 2011, **11**, 723-726.
- 17 J. Garcia-Cordero, D. Kurzbuch, F. Benito-Lopez, D. Diamond, L. Lee, and A. Ricco, *Lab on a chip*, 2010, **10**, 2680-2687.
- 18 A. Venancio-Marques, F. Barbaud, and D. Baigl, *Journal of the American Chemical Society*, 2013, **135**, 3218-3223.
- 19 X. Miao, B. Wilson, and L. Lin, *Applied Physics Letters*, 2008, **92**, 124108.
- 20 H. Sun, M. Yu, G. Wang, X. Sun, and J. Lian, *The Journal of Physical Chemistry C*, 2012, **116**, 9000-9008.
- 21 A. Tesler, L. Chuntonov, T. Karakouz, T. Bendikov, G. Haran, A. Vaskevich, and I. Rubinstein, *The Journal of Physical Chemistry C*, 2011, **115**, 24642-24652.
- 22 G. Longobucco, G. Fasano, M. Zharnikov, L. Bergamini, S. Corni, and M. Rampi, *Sensors and Actuators B: Chemical*, 2014, **191**, 356-363.
- 23 D. Duffy, J. McDonald, O. Schueller, and G. Whitesides, *Analytical chemistry*, 1998, **70**, 4974-4984.
- 24 Z. Fang, Y.-R. Zhen, O. Neumann, A. Polman, F. Abajo, P.

- Nordlander, and N. Halas, *Nano letters*, 2013, **13**, 1736-1742.
- 25 S. -Z. Li, R. Chen, H. Wang, Q. Liao, X. Zhu, and Z. -B. Wang, *Applied Thermal Engineering*, 2014, **64**, 129-138.
- 26 W. Brevis, Y. Niño, and G. H. Jirka, *Experiments in Fluids*, 2011, **50**, 135-147.
- 27 W. Al-Faqheri, F. Ibrahim, T. Thio, J. Moebius, K. Joseph, H. Arof, and M. Madou, *PLoS one*, 2013, **8**, e58523.
- 28 A. Atwe, A. Gupta, R. Kant, M. Das, I. Sharma, and S. Bhattacharya, *Microsystem Technologies*, 2014, **20**, 1373-1381.
- 29 C. Fang, L. Shao, Y. Zhao, J. Wang, and H. Wu, *Advanced Materials*, 2012, **24**, 94-98.
- 30 J Zeng, D Banerjee, M Deshpande, and JR Gilbert, *Micro Total Analysis Systems 2000. Springer Netherlands*, 2000, 579-582.
- 31 AL Tiensuu, O Öhman, and L Lundblad, *Micro Total Analysis Systems 2000. Springer Netherlands*, 2000: 575-578.
- 32 J.-M. M. Park, Y.-K. K. Cho, B.-S. S. Lee, J.-G. G. Lee, and C. Ko, *Lab on a chip*, 2007, **7**, 557-564.
- 33 G. Baffou, J. Polleux, H. Rigneault, and S. Monneret, *The Journal of Physical Chemistry C*, 2014, **118**, 4890-4898.
- 34 X. Mao, B. Juluri, M. Lapsley, Z. Stratton, and T. Huang, *Microfluidics and Nanofluidics*, 2009, **8**, 139-144.
- 35 S. Wang, Z. Jiao, X. Huang, C. Yang, and N. Nguyen, *Microfluidics and Nanofluidics*, 2008, **6**, 847-852.
- 36 K. Zhang, A. Jian, X. Zhang, Y. Wang, Z. Li, and H.-Y. Tam, *Lab on a chip*, 2011, **11**, 1389-1395.
- 37 Technical sheet: Molecular Probes Live/Dead BacLight™ bacteria viability kit technical sheet. Molecular Probes Inc., 1995.